Interfacial Charge-Transfer Enhances the Dual-Function of Porous NiCo$_2$S$_4$@SiO$_2$ Heterojunction for High-Performance Li-S Batteries

Shuangqing Fan, [‡*a] Hao-Qiang Cao, [‡b] Jianjun Song,[c] Minghui Cao,[a] and Jie Sua,[*]

[a]*School of Electronic and Information Engineering, Qingdao University, Qingdao 266071, China*

[b]*Chinese Automotive Technology & Research Centre, Tianjin 301822, China*

[c]*College of Physics, Qingdao University, Qingdao 266071, China*

[‡]*S. Fan, and H. Cao contributed to this work equally.*

*E-mail: jsu@qdu.edu.cn, sqfan@qdu.edu.cn

Experimental Section

Materials synthesis:

The NiCo@SiO$_2$ hybrid precursor was prepared by a hydrothermal method. Typically, 4 mmol CoCl$_2$·6H$_2$O, 2 mmol NiCl$_2$·6H$_2$O, and 20 mmol urea were dissolved in 40 mL of DI water. Then 0.75 mL tetraethyl orthosilicate (TEOS) was added to the mixture and sonicated in a bath for 30 min. The content was then transferred to a 50 mL Teflon-lined stainless-steel autoclave and heated at 120 °C for 6 h. The gray precipitate was obtained by centrifuging and rising with DI water and ethyl alcohol three times. Afterward, the porous coral globular NiCo$_2$S$_4$@SiO$_2$ was obtained by placing NiCo@SiO$_2$ hybrid precursor in a 50 mL Teflon container with an aqueous solution of 2 mmol Na$_2$S·9H$_2$O. The autoclave was put into an electric oven and heat at 120 °C for 6 h. Finally, the dark precipitate was collected by centrifugation, and vacuum dried at 60 °C to obtain the NiCo$_2$S$_4$@SiO$_2$. The preparation method of NiCo$_2$S$_4$ was the same as described for NiCo$_2$S$_4$@SiO$_2$, except that no TEOS was added.

NiCo$_2$S$_4$@SiO$_2$/S or NiCo$_2$S$_4$/S cathode materials were synthesized using classical melt diffusion methods. Briefly, NiCo$_2$S$_4$@SiO$_2$ or NiCo$_2$S$_4$ and pure sulfur (2:8 in m/m) were ground together. The composite was heated at 155 °C for 10 h in a porcelain boat, and then heat up to 200 °C for 30 min to cause diffusion of the sulfur into host materials.

The lithium polysulfide (Li$_2$S$_6$) solution was prepared by adding sulfur and Li$_2$S (5:1 molar ratio) to the DME/DOL ((1:1, v/v) solvent in an Ar-filled glove box. Then the mixture was stirred at 60 °C for 1 day to form Li$_2$S$_6$ solution.

Materials characterization

XRD patterns of NiCo$_2$S$_4$@SiO$_2$ and NiCo$_2$S$_4$ were defined using Bruker D8 Advance X-ray diffractometer (Cu Kα, λ = 0.154 nm). The morphology and structure were characterized using FESEM (Hitachi S-4800), field-emission TEM (JEOL 3010 microscope). The chemical states were analyzed by XPS (ESCALAB 250Xi). The chemical content was analyzed on a Shimadzu TGA-50 instrument from room temperature to 800 °C at a heating rate of 10 °C/min in N$_2$ atmosphere. Fourier transform infrared (FTIR) characterization was recorded on Agilent Cary 600 series FTIR spectrometer.

Electrochemical Characterization

Symmetric electrochemical cells were assembled as follows: NiCo$_2$S$_4$@SiO$_2$ and PVDF (9:1 in m/m) were homogenized in NMP and coated on an Al foil. The foil was then dried in vacuum oven and cut into 1 cm diameter circles. Two of identical NiCo$_2$S$_4$@SiO$_2$ electrode sheets, a Celgard 2400 seperator, and 30 μL of an 0.2 M Li$_2$S$_6$ electrolyte were assembled into a CR2032 cell. The CV measurements were carried out at various scan rates in the potential range of -1.0 to 1.0 V. The Li-S batteries were constructed differently: a slurry of 70 wt% active material (NiCo$_2$S$_4$@SiO$_2$/S, NiCo$_2$S$_4$/S), 20 wt% carbon black, and 10 wt% PVDF binder in NMP was coated to Al foil. The NiCo$_2$S$_4$@SiO$_2$/S or NiCo$_2$S$_4$/S as a cathode with Li foil as an anode, together with Celgard 2400 as a separator, and 1 M LiTFSI in a DOL/DME mixture (1:1 v/v) as electrolyte, was assembled into CR2032 coin cell. Galvanostatic charge/discharge tests were conducted in the window of 1.7-2.8 V in LAND CT2001 equipment. The electrochemical impedance spectroscopy (EIS) measurements were carried out in the frequency range of 0.01 Hz to 100 kHz in the fully charged state. The CV and EIS tests were carried out on an electrochemical workstation (IviumStat.h).

Electrical conductivity was measured in air by four-probe technique using a DC standard voltage/current generator (SB118) and a precision digital multimeter (PZ158A) at room temperature.

Computational Methods

The electronic structures and energy were computed by Vienna ab initio Simulation package (VASP) of density functional theory (DFT). The projector augmented wave (PAW) model with Perdew−Burke−Ernzerhof (PBE) function was employed to describe the interactions between core and electrons. An energy cutoff of 400 eV was used for the plane wave expansion of the electronic wave function. The Brillouin zones of all systems were sampled with gamma-point centered Monkhorst-Pack grids. A 2×2 ×1 Monkhorst Pack k-point setup was used for slab geometry optimization. The force and energy convergence criterion were set to 0.02 eV Å^{-1} and 10^{-5} eV, respectively.
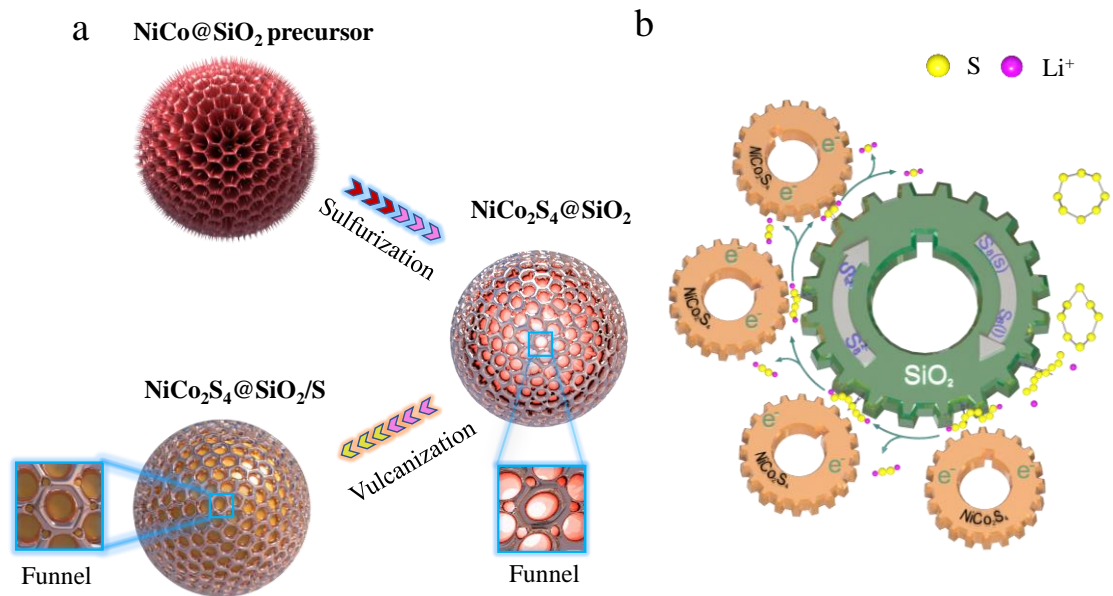
Fig. S1. Schematic diagram of a) synthesis process of $NiCo_2S_4@SiO_2/S$ composite, b) the discharge process at the $NiCo_2S_4@SiO_2/S$ cathode.

The as-prepared $NiCo@SiO_2$ precursor is vulcanized by hydrothermal method with sodium sulfide nonahydrate to form open-hole hollow coral-like $NiCo_2S_4@SiO_2$ sphere, which contain two main size mesoporous. Then sulfur can melt diffusion and fill into these mesoporous. The $NiCo_2S_4@SiO_2$ trapped sulfur can progress the electrochemical reaction according to the diagram in Fig. S1b. The solid sulfur stored in the mesoporous of the host forms solvated sulfur molecules first, followed by the ring-opening reaction and receiving electrons from $NiCO_2S_4$ and Li^+ from anodes. In this sense, the high conductivity and charge density of $NiCo_2S_4$ can enhance the redox electron transfer, and accelerate the polysulfide conversion. Meanwhile, the oxygen groups on silica can serve as Li^+ tethering sites and transfer medium to fast the kinetics. The immobilizing polysulfide chains on Li^+ is more important to inhibit the polysulfide shuttle effect and form low-order polysulfides.[1]
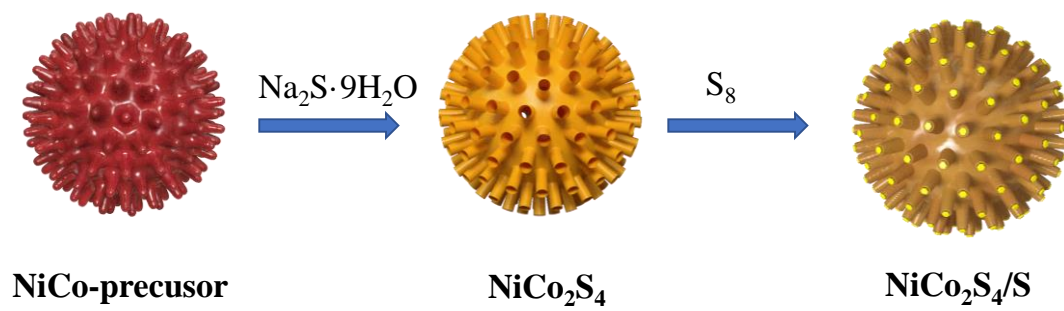
$Na_2S \cdot 9H_2O$ S_8

NiCo-precusor   **NiCo$_2$S$_4$**   **NiCo$_2$S$_4$/S**

Fig. S2. Schematic illustration of the synthesis of the NiCo$_2$S$_4$/S composite.
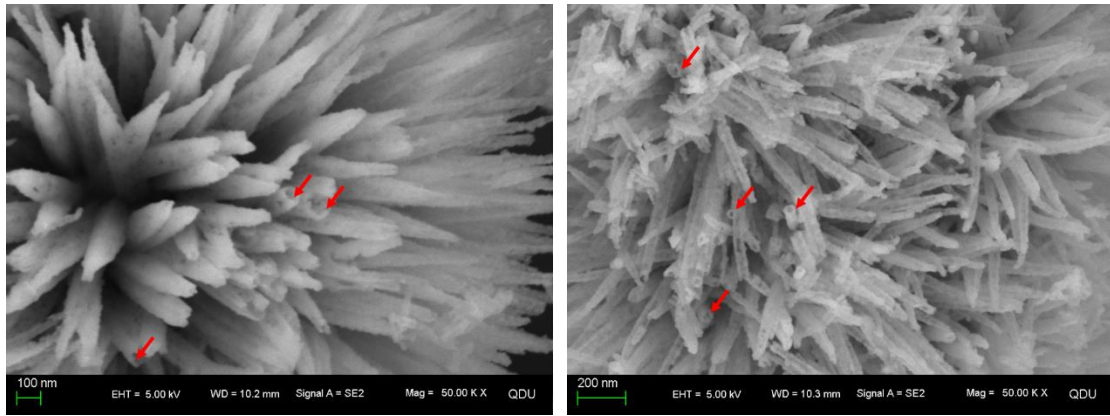
Fig. S3. Typical SEM image of $NiCo_2S_4$.
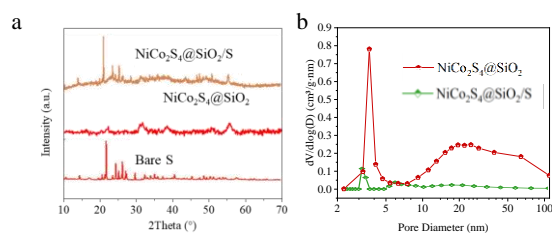
Fig. S4. a) XRD patterns of NiCo$_2$S$_4$@SiO$_2$, NiCo$_2$S$_4$@SiO$_2$/S composite, and bare sulfur. The XRD patterns of NiCo$_2$S$_4$@SiO$_2$/S composites show the peaks of sulfur and as-prepared NiCo$_2$S$_4$@SiO$_2$, respectively. **b)** Pore size distributions of NiCo$_2$S$_4$@SiO$_2$, NiCo$_2$S$_4$@SiO$_2$/S. After the filling of sulfur, the BET surface area and pore volume of NiCo$_2$S$_4$@SiO$_2$/S composites decreased to 13 m^2 g^{-1} and 0.1 cm^3 g^{-1}, indicating that most of the pores are occupied by sulfur in accordance with XRD measurements.

Fig. S5. Photograph of the Li_2S_6 solution, Li_2S_6-$NiCo_2S_4@SiO_2$ solution, and Li_2S_6-$NiCo_2S_4$ solution before and after 6 h standing.

To evaluate the adsorption capacity of $NiCo_2S_4$ and $NiCo_2S_4@SiO_2$ with the LiPSs, adsorption experiment was conducted under Ar atmosphere. After mixing the $NiCo_2S_4$ and $NiCo_2S_4@SiO_2$ with Li_2S_6 solution and standing for 2h, the color of the sample with $NiCo_2S_4@SiO_2$ became almost colorless, while tan color still remained in the vial with $NiCo_2S_4$ as displayed in Fig. S4. This demonstrates that the polar $NiCo_2S_4@SiO_2$ composites have a stronger adsorption of polysulfides compared to $NiCo_2S_4$.

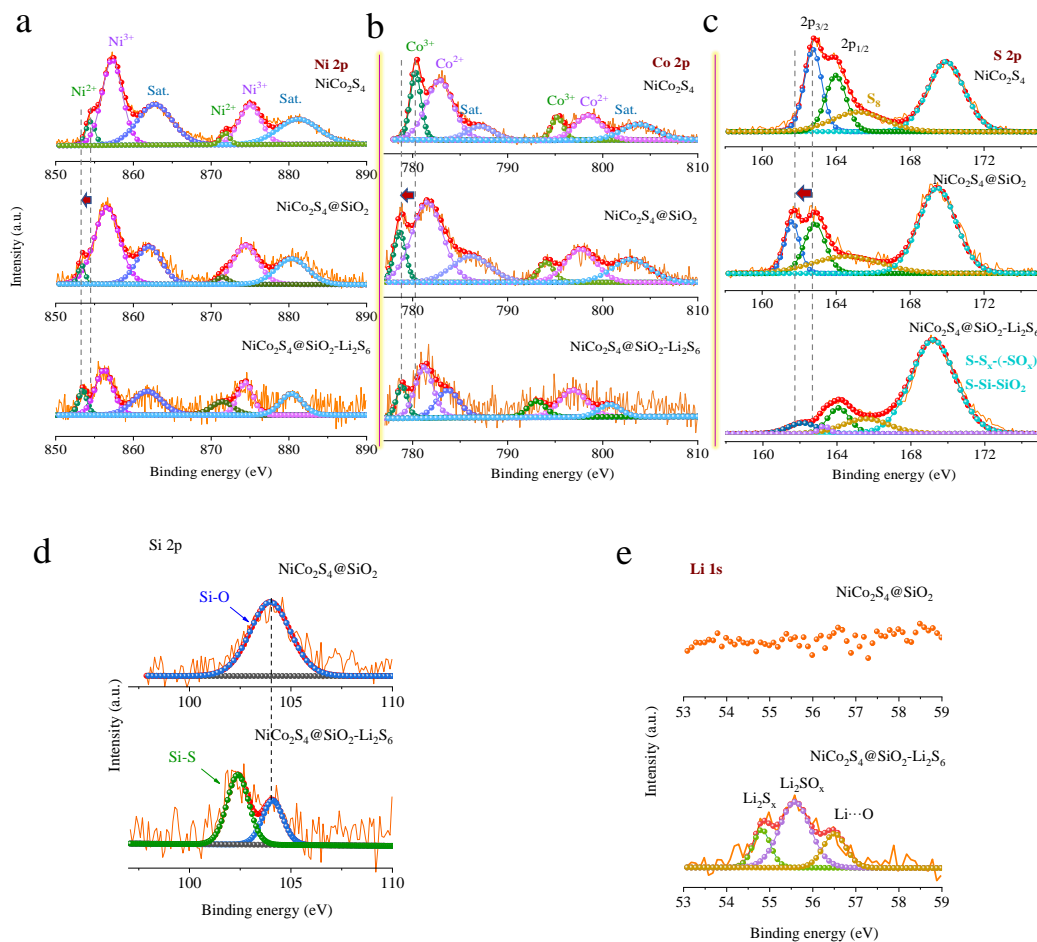**Fig. S6.** High-resolution XPS spectra of a) Ni 2p, b) Co 2p), c) S 2p, d) Si 2p and e) Li 1s of the $NiCo_2S_4$, and $NiCo_2S_4@SiO_2$ before and after absorbing Li_2S_6.

There is a new peak emergent at 102.3 eV in the Si 2p spectrum due to the S_6^{2-} that fills the oxygen vacancy and is coordinated with the Si^+ sites, resulting in the formation of Si–S bonds (Fig. S6d, ESI[†]).[14] The opposite surface charge on the SiO_2 surface will separate lithium salt into Li^+ cationics that are absorbed on the Si–O[−] groups, and S_x^{2-} anions that are supposed to be adsorbed at the hydroxyl phase (Fig. S7b, ESI[†]). Therefore, a strong Li 1s signal is detected, as shown in the Fig. S6e (ESI[†]). The Li 1s spectrum is split into three peaks: Li–S_x, Li–SO_x, and Li–O coordinate bond peaks with the binding energies of 54.8, 55.6, and 56.5 eV, respectively. The silica substrate plays a crucial role in chemical anchoring to restrict the shutting effect of LiPSs, thus making the ultrastable performance of Li–S battery possible. In addition, the Lewis acid–base interactions among Li^+ and SiO_x will effectively order the ions into the 3D nanotube channels and then shorten the distance of Li^+ transfer.
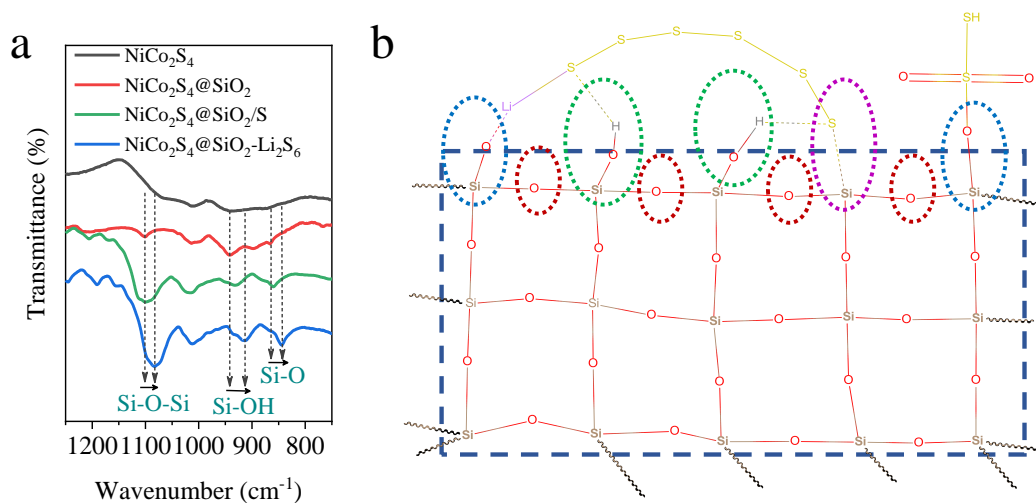
Fig. S7. a) FTIR spectra of the $NiCo_2S_4$, $NiCo_2S_4@SiO_2$, $NiCo_2S_4@SiO_2$-Li_2S_6, and $NiCo_2S_4@SiO_2$/S. b) Schematic diagram of Li_2S_6 adsorption on SiO_2 and the resulting chemical bond.

The bending vibration signal at 943 cm^{-1} are attributed to polar silanol (Si-OH) vibration. And the other two peaks around 1102.3 and 864.6 cm^{-1} are assigned to symmetric and asymmetric stretching vibration of Si-O-Si. They reveal that silica ends up with silanol groups, which induce the silica surface polarity.[2]

The bending vibration signal at 943 cm^{-1} are attributed to polar silanol (Si-OH) vibration. The association of $NiCo_2S_4@SiO_2$ and Li_2S_6 generally results in a considerable redshift of the IR transmittance bands, originating from the strong interaction such as hydrogen bond, Li-O bond, and SO_x-Si as well as S_x^{2-}-Si$^+$ electrostatic interactions between the Li_2S_6 and the oxygen-rich surface of the silica (Fig. S7b), consistent with the XPS results. consistent with the XPS results. The above-mentioned results triggered us to believe that polar silica has an efficient intermolecular interaction with polysulfides. Additionally, the adsorption capacity would be further enhanced after negative charge-transfer from silica to NiCo2S4.
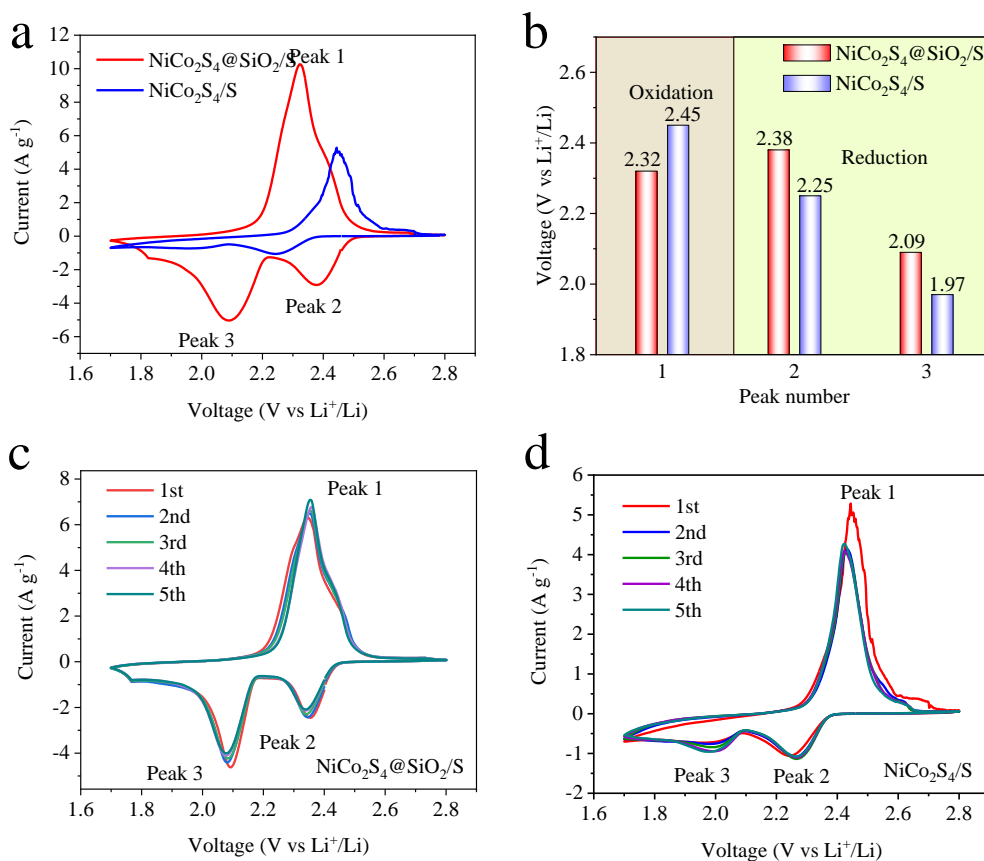
Fig. S8. a) CV curves of the NiCo$_2$S$_4$@SiO$_2$/S and NiCo$_2$S$_4$/S cathodes at 0.1 mV s^{-1}. b) The comparison of corresponding onset potentials of peaks (1, 2, and 3) of the NiCo$_2$S$_4$@SiO$_2$/S and NiCo$_2$S$_4$/S cathodes c, d) CV profiles of the NiCo$_2$S$_4$@SiO$_2$/S and NiCo$_2$S$_4$/S cathodes for the initial seven cycles at 0.1 mV s^{-1}.

The peaks at 2.09 and 2.38 V during the first discharge process are attributed to the reduction conversion of sulfur to lithium polysulfide (Li$_2$S$_x$, 4<x<8) and then to insoluble lithium sulfide (Li$_2$S$_2$/Li$_2$S), while the peak at 2.32 V corresponds to the multistep oxidation conversion of Li$_2$S$_2$/Li$_2$S to polysulfide and further to sulfur. Comparatively, the reduction and oxidation peaks of the NiCo$_2$S$_4$/S electrode show a serious decrease in the peak intensity. In addition, a significant peak broadening and lower potential shift of the reduction peaks for NiCo$_2$S$_4$@SiO$_2$/S are observed than that of NiCo$_2$S$_4$/S. In contrast, the oxidation peak of NiCo$_2$S$_4$@SiO$_2$/S shifts to the positive potential.

11

Table S1. A list of calculated diffusion coefficient of lithium ions (D_{Li+}, cm^2 s^{-1})

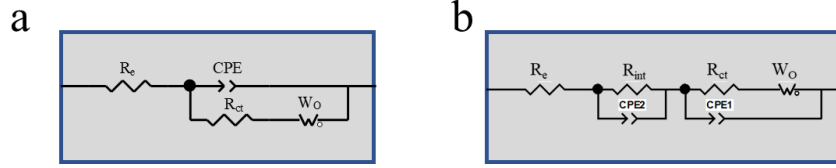| Sample	Peak 1 (Li$_2$S→S8)	Peak 2 (S8→Li$_2$S$_4$)	Peak 3 (Li$_2$S$_4$→Li$_2$S)
NiCo$_2$S$_4$@SiO$_2$	**6.19×10^{-7}**	**1.39×10^{-7}**	**1.19×10^{-7}**
NiCo$_2$S$_4$	8.63×10^{-8}	3.23×10^{-8}	1.07×10^{-8}

Fig. S9. The equivalent electric circuit diagram of the fresh and 200th cycled NiCo$_2$S$_4$@SiO$_2$/S and NiCo$_2$S$_4$/S cathodes in Li-S batteries.

The Li$^+$ diffusion properties can be evaluated from the following equation 1 and 2.

$$D_{Li}^+ = \frac{R^2 T^2}{2A^2 n^4 F^4 C^2 \sigma} \tag{1}$$

$$Z` = R_e + R_f + R_{ct} + \sigma\omega^{-1/2} \tag{2}$$

R is gas constant, T represents absolute temperature, F is Faraday constant, and σ is the Warburg factor.

Table S2. Electrode resistance obtained from the equivalent circuit fitting of the $NiCo_2S_4@SiO_2/S$ and $NiCo_2S_4$ /S cathodes

Sample	Cycle	$R_e(\Omega)$	$R_{ct}(\Omega)$	$W_e(\Omega)$
$NiCo_2S_4@SiO_2$		**1.2**	**43.2**	**39.5**
	Before cycling			
$NiCo_2S_4$		2.2	57.6	46.3

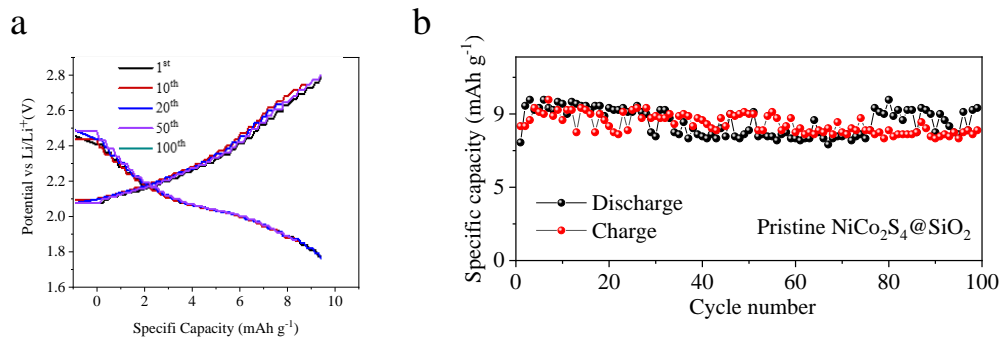| Sample	Cycle	$R_e(\Omega)$	$R_{ct}(\Omega)$	$W_e(\Omega)$
$NiCo_2S_4@SiO_2$		**1.6**	**15.2**	**36.2**
	200th cycling			
$NiCo_2S_4$		2.5	32.2	43.7

Fig. S10. a) Discharge-charge profiles and b) cycle performance of the pure NiCo$_2$S$_4$@SiO$_2$ electrode.
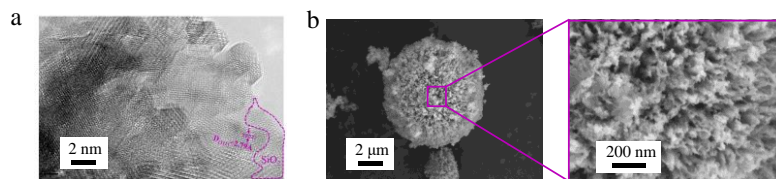
Fig. S11. **a)** HR-TEM image of NiCo$_2$S$_4$@SiO$_2$/S composite after 50 cycles. It can be clearly observed that the structures of NiCo$_2$S$_4$ and SiO$_2$ are maintained well after the cycle. b) SEM images of overall NiCo$_2$S$_4$@SiO$_2$/S cathode with different magnification after 50 cycles at 2 C show the well-integrated microspheres are perfectly maintained, confirming that the NiCo$_2$S$_4$@SiO$_2$ can preserve structural integrity of the active sulfur upon prolonged cycling.
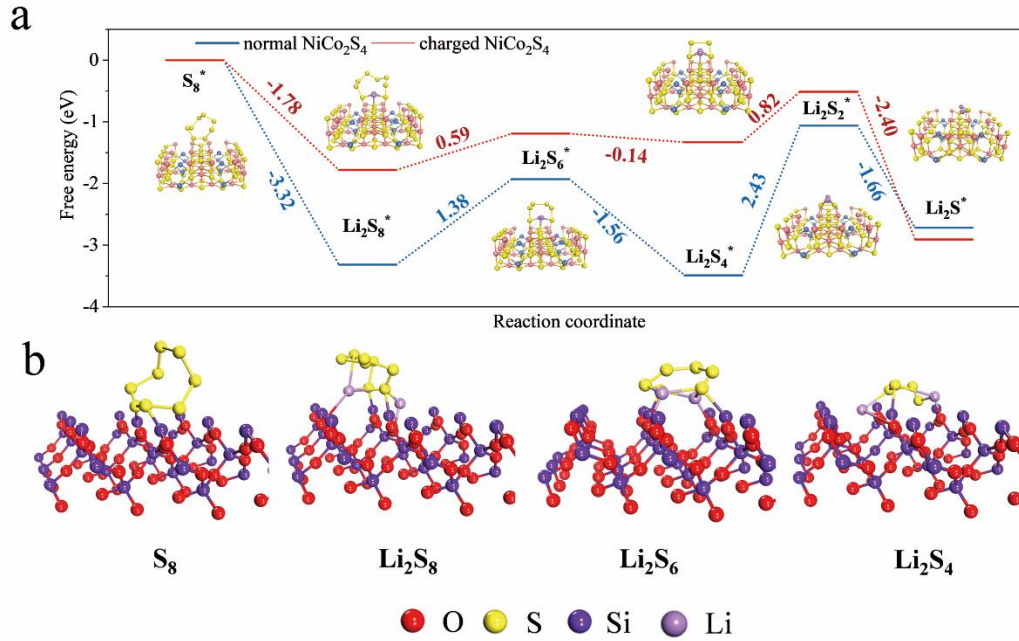
Fig. S12. a) Energy profiles for the discharge reaction of LiPSs on SiO₂ substrates. (lavender ball: Li atom; yellow ball: S atom; pink ball: Co atom; blue ball: Ni atom). b) Calculated adsorption energies of S_8, Li_2S_8, Li_2S_6, and Li_2S_4 species adsorption on the SiO_2 (001) planes.

We calculated the reduction pathways of LiPSs on the (400) surface of electron rich $NiCo_2S_4$ and normal $NiCo_2S_4$, and the binding strength of LiPSs and SiO_2 with and without net negative charge, respectively. We calculated the binding energy between polysulfides and silica. As shown in Fig. S12b, the binding energies of S_8, Li_2S_8, Li_2S_6, and Li_2S_4 on the surface of normal silica (001) planes are -2.65 eV, -5.34 eV, -9.98 eV, -7.67 eV, respectively, which is more negative than that with negatively charged silica (-1.75 eV, -4.18 eV, -9.21 eV, -6.65 eV). This result suggests that silica shows improved functions for trapping polysulfides after the negative charge transfer from silica to $NiCo_2S_4$. The weak adsorption of negatively charged SiO_2 and $NiCo_2S_4$ is due to electrostatic repulsion with the anionic polysulfide species.

Table S3. A comparison of electrochemical performance of $NiCo_2S_4@SiO_2/S$ composite in this work with other NiCoS-based nanophase materials or other mesoporous silica electrodes in Li-S batteries.

Materials	Sulfur loding (mg cm^{-2})	Rate (C, mA cm^{-2})	Reversible Capacity (mAh g^{-1} mAh cm^{-2})	Capacity after cycling (mAh g^{-1} mAh cm^{-2})	Ref.
$NiCo_2S_4@C$ (interlayer)	~1	1.0 C	880	700 mA (200th)	3
NiCoS/PP-P (interlayer)	~1.5	0.2	1041	765 (100th)	4
$NiCo_2S_4$ (interlayer)	-	0.5	923	836 (500th)	5
$NiCo_2S_4$	1.1	0.5	878.4	318.9 (500th)	6
$NiCo_2S_4@CNTs/S$	0.8	0.5	1028	940 (50th)	7
S/NF@NCS-30	1.5	0.5	808.61	490.03(150th)	8
NiS@ C-HS	1.0	0.2	1002	718 (200th)	9
$NiCo_2S_4$ nanorod/S	1.0	0.1	1028	421(100th)	10
$NiCo_2S_4/S$	1.5	0.2	1137	816 (350th)	11
$Si/SiO_2/C$	3.1	2	836	610(500th)	12
pOMS	2	0.2	1159	974(200th)	13
fiber@SiO_2 (interlayer)	0.7	1.0	963.2	618.4 (500th)	14
PP-SiO_2 (interlayer)	1.2	0.2	937	603.5(200th)	15
$NiCo_2S_4@SiO_2/S$	1.5	1	1258	951(660th)	This work
	4.1	0.2	1135	976 (120th)	

References

1   J. Li, H. Zhang, L. Luo, H. Li, J. He, H. Zu, L. Liu, H. Liu, F. Wang and J. Song, *Journal of Materials Chemistry A*, 2021, **9**, 2205–2213.

2   Y. Lin, X. Wang, J. Liu and J. D. Miller, *Nano Energy*, 2017, **31**, 478–485.

3   B. Li, Y. Pan, B. Luo, J. Zao, Y. Xiao, S. Lei and B. Cheng, *Electrochimica Acta*, 2020, **344**, 135811.

4   S. Huang, Y. Wang, J. Hu, Y. Von Lim, D. Kong, L. Guo, Z. Kou, Y. Chen and H. Y. Yang, *NPG Asia Materials*, 2019, **11**, 1–12.

5   B. Liu, S. Huang, D. Kong, J. Hu and H. Y. Yang, *Journal of Materials Chemistry A*, 2019, **7**, 7604–7613.

6   X. Tan, X. Wang, X. Wang, Y. Wang, C. Li and D. Xia, *Ionics*, 2019, **25**, 4047–4056.

7   X. Lu, Q. Zhang, J. Wang, S. Chen, J. Ge, Z. Liu, L. Wang, H. Ding, D. Gong, H. Yang, X. Yu, J. Zhu and B. Lu, *Chemical Engineering Journal*, 2019, **358**, 955–961.

8   C. Yang, X. Wang, G. Liu, W. Yu, X. Dong and J. Wang, *Journal of Colloid and Interface Science*, 2020, **565**, 378–387.

9   C. Ye, L. Zhang, C. Guo, D. Li, A. Vasileff, H. Wang and S. Z. Qiao, *Advanced Functional Materials*, 2017, **27**, 1–9.

10 L. Wu, S. Tang and R. Qu, *Journal of Materials Science: Materials in Electronics*, 2019, **30**, 189–199.

11 S. Li, P. Xu, M. K. Aslam, C. Chen, A. Rashid, G. Wang, L. Zhang and B. Mao, *Energy Storage Materials*, 2020, 27, 51–60.

12 S. Rehman, S. Guo and Y. Hou, *Advanced Materials*, 2016, **28**, 3167–3172.

13 B. J. Lee, T. H. Kang, H. Y. Lee, J. S. Samdani, Y. Jung, C. Zhang, Z. Yu, G. L. Xu, L. Cheng, S. Byun, Y. M. Lee, K. Amine and J. S. Yu, *Advanced Energy Materials*, 2020, **10**, 1–14.

14 T. Liu, X. Sun, S. Sun, Q. Niu, H. Liu, W. Song, F. Cao, X. Li, T. Ohsaka and J. Wu, *Electrochimica Acta*, 2019, **295**, 684–692.

15 J. Li, Y. Huang, S. Zhang, W. Jia, X. Wang, Y. Guo, D. Jia and L. Wang, *ACS Applied Materials and Interfaces*, 2017, **9**, 7499–7504.